

Facile Spray Drying Route for the Three-Dimensional Graphene-Encapsulated Fe₂O₃ Nanoparticles for Lithium Ion Battery Anodes

Guan-Wei Zhou,[†] Jiulin Wang,[†] Pengfei Gao,[†] Xiaowei Yang,[§] Yu-Shi He,^{*,†,§} Xiao-Zhen Liao,[†] Jun Yang,[†] and Zi-Feng Ma^{†,‡}

[†]Institute of Electrochemical and Energy Technology, Department of Chemical Engineering, Shanghai Jiao Tong University, Shanghai, 200240, China

[‡]State Key Laboratory of Metal Matrix Composites, Shanghai Jiao Tong University, Shanghai 200240, PR China

[§]Department of Materials Engineering, Monash University, VIC 3800, Australia

S Supporting Information

ABSTRACT: Crumpled graphene sheet-wrapped nano-Fe₂O₃ (Fe₂O₃@GS) composites with a three-dimension (3D) hierarchical structure have been made by a facile and efficient spray drying route with a following mild heat reduction in air. In the as-obtained composites, the crumpled GS around Fe₂O₃ particles could not only provide a 3D conductive matrix but also buffer the volume change of Fe₂O₃. Fe₂O₃ particles which evenly distribute in the crumpled GS could also act as spacers to avoid the close restacking of GS. Compared to the bare Fe₂O₃, the Fe₂O₃@GS composites as Li ion battery anodes show dramatically improved electrochemical performance including cyclic stability and rate capability owing to the special encapsulated structure and the excellent synergistic effect between the two components.

1. INTRODUCTION

Transition metal oxides have been considered as promising anode materials for rechargeable Li-ion batteries (LIBs) with high theoretical capacity compared to that of conventional graphite (372 mA h g⁻¹).¹ Among of them, hematite Fe₂O₃ (α -Fe₂O₃) was paid much attention because of its low processing cost and environmental friendliness.^{2,3} However, the poor cycling performance of Fe₂O₃, especially at high rates, has hindered its practical application. It is partly related to the drastic volume fluctuation (>200%) upon the insertion and extraction of Li ions, which could cause electrode pulverization and loss of electrical continuity, leading to rapid capacity loss.⁴ Carbon-coated nanostructured Fe₂O₃ composites have been attractive options to alleviate the problem.^{5–10} However, the stiff carbon framework would crack upon the huge volume expansion.¹¹ A flexible carbon coating that can provide enough buffer is thus needed.

Graphene, a newly discovered two-dimension (2D) material, has recently attracted a great deal of research interest due to its superior mechanical flexibility, high electrical conductivity, large specific surface area, and so on.^{12–14} As a modified component, graphene has been introduced into various inorganic and organic materials to form functional composites for LIBs.^{9,15–32} The main problem in the preparation of the graphene-based composites focuses on how to effectively reduce the agglomeration and restacking of GS to fully harness the unique properties of individual graphene sheet. The conventional direct high-temperature calcination could easily result in severe agglomeration of the GS.³³ More recently many efforts have been made for maintaining the structure of graphene network, such as keeping the graphene solvated^{34,35} and developing a range of 3D graphene-based composites.^{36–41}

The spray drying technique has been widely used for nanoparticle encapsulation in the chemical and food industries owing to its low cost, simple apparatus and easy scale-up for mass production.^{42,43} With the help of the method, 2D aqueous graphene oxide (GO) sheets can be converted to 3D crumpled and flexible graphene particles which are very aggregation-resistant by capillary compression.^{44,45} Spray drying is inferential to be a suitable synthetic method for preparing 3D graphene-based composites. Here, 3D crumpled graphene sheet-wrapped nano-Fe₂O₃ (Fe₂O₃@GS) composites have been prepared by a simple spray drying process and a following mild thermal reduction in air. The method offers significant advantages in preparation because no surfactant, filtration or washing processes, high-temperature calcination, or protective atmosphere are required. Our experimental results reveal that, compared with pristine Fe₂O₃, the Fe₂O₃@GS composites as LIB anodes demonstrate greatly improved cyclic stability and excellent rate capability. Most importantly, such a facile and green synthesis strategy could be applicable for the large-scale production of 3D graphene-based composites.

2. EXPERIMENTAL SECTION

Synthesis of Fe₂O₃ Nanoparticles and Fe₂O₃@GS Composites. The Fe₂O₃ nanoparticles were synthesized based on a hydrothermal method.⁴⁶ Briefly, FeCl₃·6H₂O (0.225g) was dissolved in 30 mL deionized water, followed by adding 28% aqueous solution of ammonia slowly to adjust the pH to 8. Then, the mixture was transferred into a Teflon-

Received: September 13, 2012

Revised: December 3, 2012

Accepted: December 18, 2012

Published: December 18, 2012



lined autoclave and heated at 180 °C for 24 h. After reaction, the autoclave was left to cool down to the room temperature naturally. The resulting Fe₂O₃ precipitate was washed with distilled water several times, collected, and dried in an oven at 80 °C overnight.

Graphite oxide was synthesized from natural graphite powder (Grade 230, Asbury Carbons) using the modified Hummers method.³⁴ The as-prepared graphite oxide was exfoliated into deionized water by ultrasonication to form graphene oxide (GO) suspension. Thereafter, a certain amount of nano-Fe₂O₃ powder was added into the GO suspension (1 mg mL⁻¹) in a weight ratio of Fe₂O₃:GO of 8:2. The mixture was sonicated for 1 h and then spray-dried to form a Fe₂O₃@GO composite using a B-290 mini spray drier (Buchi, Swiss). The inlet air temperature at spray drying process was maintained at 200 °C. The product was collected at the vessel, and then loaded into a quartz tube in air at 220 °C for 2 h to form the Fe₂O₃@GS composite, denoted as Fe₂O₃@GS1. The Fe₂O₃@GS2 was synthesized by the same method, except that the weight ratio of Fe₂O₃:GO was 1:1. Pure Fe₂O₃ and GS samples were also prepared by the same spray drying procedure for comparison.

Structural and Morphological Characterization. X-ray photoelectron spectrometer (XPS, Kratos Axis Ultra DLD) was utilized to analyze the surface chemistries of the samples. The X-ray diffraction (XRD) measurements were carried out using a Rigaku D/MAX-2200/PC X-ray diffractometer at 40 kV and 20 mA, with a Cu K α radiation source. Raman spectroscopy was used to identify the surface characteristics of the samples using a BRUKER optic SENTERRA (R-200L) with the laser wavelength of 633 nm at room temperature. Thermogravimetric analysis (TGA) was performed using a STA 449F3 analyzer (NETZSCH Co., Germany) to evaluate the residual level of Fe₂O₃@GS composites after calcination. The morphology and microstructure of the samples were monitored using a FEI Nova SEM 230 ultrahigh resolution Field Emission Scanning Electron Microscopy (FESEM) with energy-dispersive X-ray spectroscopy (EDS; INCA, Oxford) and a JEM-2010HT Transmission Electron Microscopy (TEM) (JEOL Ltd., Japan).

Electrochemical Measurements. The electrochemical performances of Fe₂O₃@GS composite, bare Fe₂O₃, and GS were evaluated under the same conditions using coin-type half cells. The working electrodes were prepared by pasting a mixture of active material, Super P conductive carbon black (40 nm, Timcal), and styrene butadiene rubber/sodium carboxymethyl cellulose (SBR/SCMC, 1:1 by weight) as binder at a weight ratio of 75:15:10. After coating the mixture onto pure Cu foil, the electrodes were dried, cut to Φ14 mm sheets, pressed at 3 MPa, and finally dried at 80 °C in vacuum for 4 h. The active materials loaded on the electrode were about 1.0–1.5 mg cm⁻². CR2016 coin cells were assembled in an argon-filled glovebox with lithium metal as counter electrode and UP3025 separator (provided by UBE Industries, Ltd., Japan). The electrolyte contained 1 M LiPF₆ in dimethyl carbonate (DMC) and ethylene carbonate (EC) mixed solvent of 1:1 (LP30 from EM Industries, Inc.). Charge–discharge cycles of the half-cells were evaluated between 0.1 and 3 V vs Li⁺/Li at room temperature using LAND CT2001A model battery test system (Wuhan Jinnuo Electronics, Ltd.) under constant current condition. The charge–discharge capacities of the composite were calculated according to the weight of Fe₂O₃@GS material in the electrode. Cyclic voltammetry (CV) measurements were carried out by using a CHI instrument

(CHI 660) at a scanning rate of 0.5 mV s⁻¹. The EIS of the cells were measured by a Solartron FRA 1260 frequency responses analyzer combined with a Solartron SI 1287 Electrochemical Interface with the ac amplitude of 10 mV over a frequency range from 100 kHz to 0.1 Hz.

3. RESULTS AND DISCUSSION

A schematic sketch of the preparation process of the 3D graphene sheets-encapsulated Fe₂O₃ nanoparticles is shown in Figure 1. First, the prepared nano-Fe₂O₃ powder is sonicated

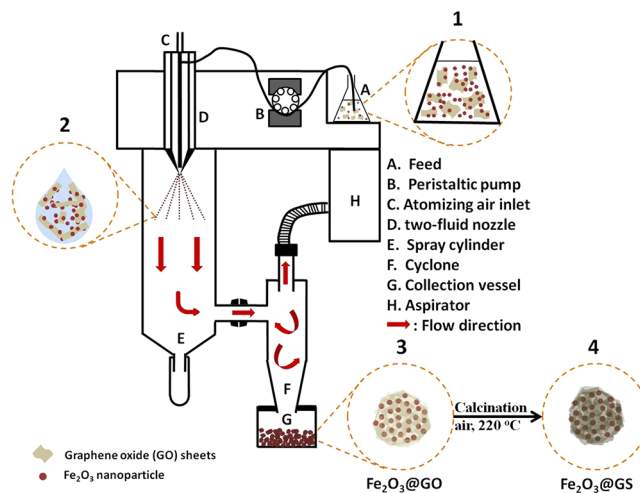


Figure 1. Schematic drawings illustrating the spray drying route and the calcination process of crumpled graphene-encapsulated Fe₂O₃ nanoparticles.

with GO in deionized water. Second, after a good aqueous dispersion is achieved, the mixture is pumped into a spray drying apparatus using a peristaltic pump and is nebulized to form aerosol droplets through a nozzle by a preheated air carrier gas. The fine droplets are subsequently dried in the cylinder. During evaporation and cooling, GO sheets can spontaneously assemble in the surface of the droplets due to their amphiphilicity and subsequently shrink and encapsulate the Fe₂O₃ nanoparticles.^{15,22,47} In addition, recent studies have confirmed that GO could be reduced at temperatures as low as about 220 °C in air atmosphere.^{48–50} So the as-formed Fe₂O₃@GO composite was further reduced by mild air calcination at 220 °C for 2 h to convert to Fe₂O₃@GS composite, which could avoid the carbothermal reduction between GS and Fe₂O₃ at high temperature in inert atmosphere. Because the GO sheets have larger lateral dimension in comparison with the Fe₂O₃ nanoparticles, the as-synthesized graphene shell would appear to be massively wrinkled and folded as a result of capillary stress.^{22,51,52}

XPS was adopted to characterize the reduction status of GO produced by the simple thermal treatment. Supporting Information Figure S1a and b indicates the C1s XPS spectra of GO before and after calcination at 220 °C for 2 h in air. Five different peaks which are corresponding to carbon sp² (C_g, ~284.8 eV), carbon sp³ (C_d, ~285.6 eV), epoxy/hydroxyl groups (C—O, ~286.4 eV), carbonyl group (C=O, ~287.3 eV), and carboxyl group (O—C=O, ~288.7 eV), respectively, are detected.^{48,50} After thermal treatment, the fraction of carbon–carbon bonding increases from 47.3% to 72.8%, and the fraction of all other oxygen levels obviously decreases. It can

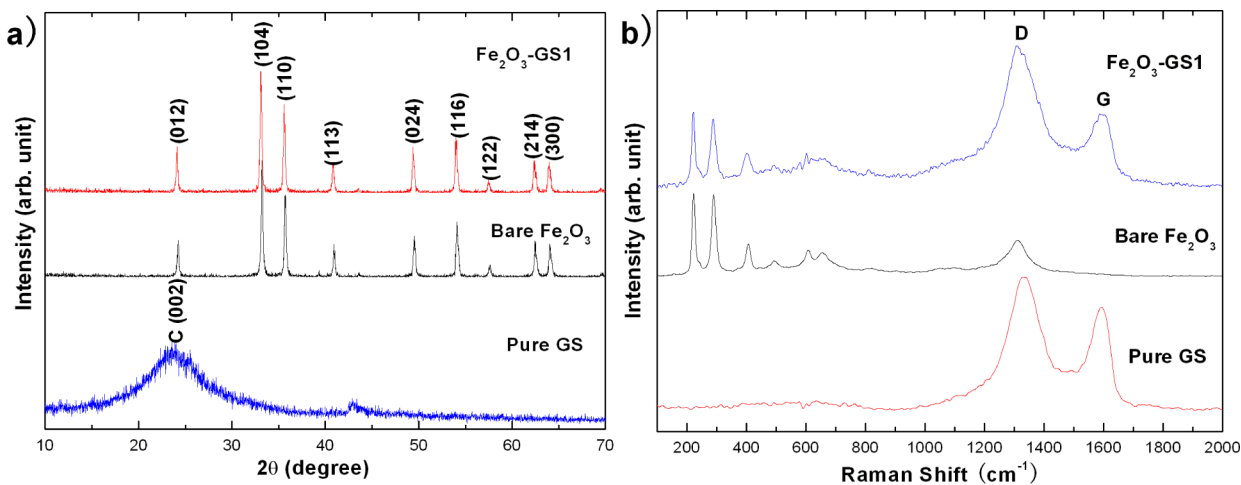


Figure 2. (a) X-ray diffraction patterns for pure GS, bare Fe_2O_3 , and Fe_2O_3 @GS1 composite. (b) Raman spectra for pure GS, bare Fe_2O_3 , and Fe_2O_3 @GS1 composite.

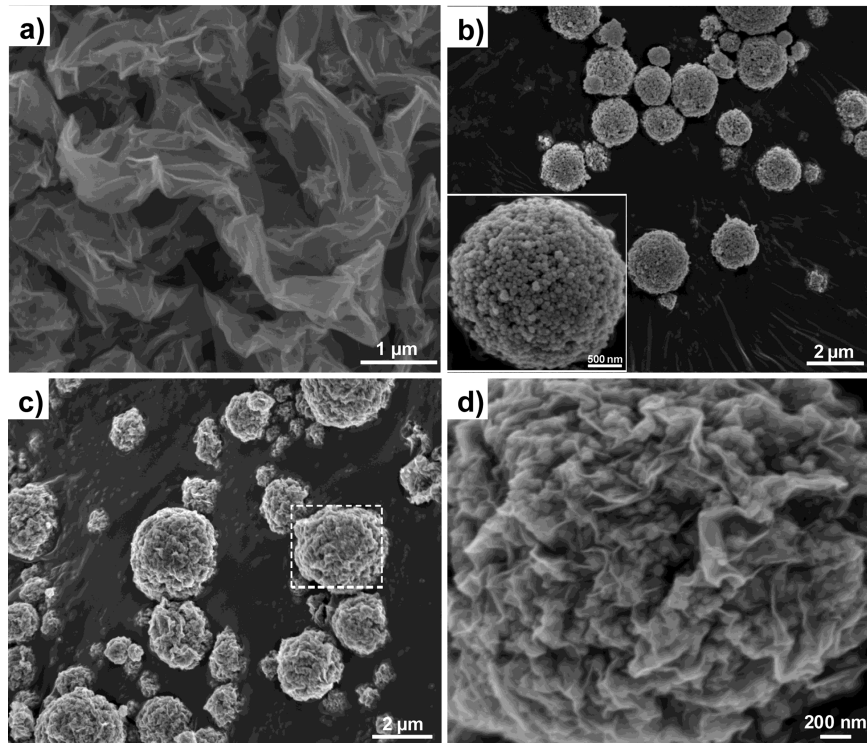


Figure 3. FESEM images of (a) pure GS, (b) bare Fe_2O_3 , and (c, d) Fe_2O_3 @GS1.

be attributed to the efficient removal of oxygen functional groups from the material and indicate the formation of graphene.⁴⁸

The X-ray diffraction (XRD) patterns of samples Fe_2O_3 @GS1, bare Fe_2O_3 , and pure GS were shown in Figure 2a. For Fe_2O_3 @GS1 composite and bare Fe_2O_3 , the major diffraction peaks match well with those of the standard hematite (JCPDS 33-0664). No obvious characteristic (002) peak of graphite at about 26° in the Fe_2O_3 @GS1 sample could be observed due to the overlap of the (012) peak of bare Fe_2O_3 at the similar degree.²⁴ Moreover, the characteristic peak of GO at about 11° is also absent in the Fe_2O_3 @GS1 composite, which suggests that GO was reduced to GS during the thermal treatment.³⁶ Figure 2b presents the Raman spectra of Fe_2O_3 @GS1, bare Fe_2O_3 and pure GS. In the Fe_2O_3 @GS1, the peaks below 1000

cm^{-1} are matched well with those of bare Fe_2O_3 . And two characteristic broad peaks at about 1310 and 1595 cm^{-1} are respectively related to the disordered D band and the graphitic G band of carbon materials,²⁶ which are in accordance with the Raman peaks of pristine GS. The intensity ratio of the D to G band ($I_D:I_G$) is clearly higher than that of pristine GS. The more disordered carbon structure in the Fe_2O_3 @GS1 could be ascribed to the insertion of Fe_2O_3 nanoparticles into graphene sheets layers.²⁰

For quantifying the amount of graphene in the Fe_2O_3 @GS composites, thermogravimetric analysis (TGA) was carried out at a heating rate of 10 °C min⁻¹ from 40 to 700 °C in air. In Supporting Information Figure S2, the weight loss at the temperature below 100 °C could be attributed to the evaporation of residual water in the samples and the rapid

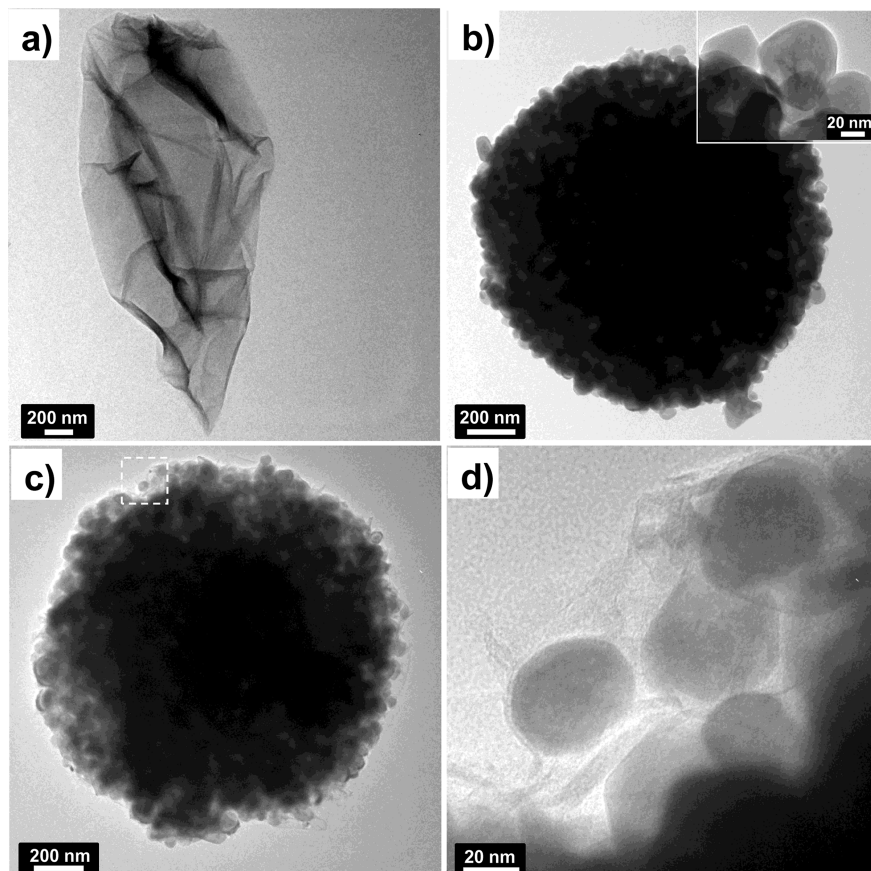


Figure 4. TEM images of (a) pure GS, (b) bare Fe_2O_3 , and (c, d) $\text{Fe}_2\text{O}_3@\text{GS}1$.

mass loss between 320 and 550 °C could be due to the combustion of the graphene.³⁵ Therefore, the weight fractions of graphene in the $\text{Fe}_2\text{O}_3@\text{GS}1$ and $\text{Fe}_2\text{O}_3@\text{GS}2$ were determined to be about 12.3% and 30.7%, respectively. FESEM images in Figure 3a–d show the surface morphologies of pure GS, bare Fe_2O_3 and $\text{Fe}_2\text{O}_3@\text{GS}1$. From Figure 3a, it could be clearly observed that the pure GS are crumpled and very stable against stretching out. The crumpled morphology could effectively prevent irreversible aggregation and restacking of GS arisen from their strong intersheet van der Waals attractions.⁴⁴ A low magnification SEM image of the bare Fe_2O_3 (Figure 3b) displays spherical secondary particles about 1–3 μm in diameter. In the inset of Figure 3b, the highly magnified image of the bare Fe_2O_3 demonstrates that the secondary particle is made of numerous smooth Fe_2O_3 nanoparticles. As shown in Figure 3c, the $\text{Fe}_2\text{O}_3@\text{GS}1$ composite also consists of sphere-like secondary particles with a similar diameter range to the bare Fe_2O_3 sample and no distinct unwrapped nanoparticle is detected. Moreover, it is obviously found from Figure 3c that the Fe_2O_3 nanoparticles are highly encapsulated in the GS matrix and the graphene shells present a typical crumpled and rippled morphology. From the result of the EDS mappings for carbon, iron, and oxygen elements (Supporting Information Figure S3), it could be observed that the Fe_2O_3 nanoparticles are uniformly distributed in the 3D crumpled graphene nanonetwork. Nevertheless, the graphene content in the $\text{Fe}_2\text{O}_3@\text{GS}$ composite could significantly influence the morphology of the product. As the graphene content increases from around 12.3% ($\text{Fe}_2\text{O}_3@\text{GS}1$) to 30.7% ($\text{Fe}_2\text{O}_3@\text{GS}2$),

the shape of the secondary particles become more irregular (Supporting Information Figure S4).

Microstructures of various samples were further characterized by TEM (Figure 4). In Figure 4a, pure GS exhibits a transparent feature with a wrinkled structure. A typical TEM image of the prepared bare Fe_2O_3 sample could be observed in Figure 4b, and the size of the Fe_2O_3 nanoparticles is about 30–100 nm with smooth surfaces. Figure 4c and d shows the TEM images of the $\text{Fe}_2\text{O}_3@\text{GS}1$ composite. As expected, the Fe_2O_3 nanoparticles are well wrapped by the graphene network and are distributed homogeneously in the network. The high-resolution TEM (HRTEM) image of the $\text{Fe}_2\text{O}_3@\text{GS}1$ composite in Supporting Information Figure S5 indicates that the Fe_2O_3 nanoparticles are encapsulated by the multiple overlapping GS. And the regular lattice fringes show a spacing of 0.25 nm, which can be assigned to the (110) plane of α - Fe_2O_3 . The flexible graphene sheets could act as a special 3D structure framework for the Fe_2O_3 nanoparticles. With the increase of the graphene content, $\text{Fe}_2\text{O}_3@\text{GS}2$ shows relatively ruleless wrapping structure (Supporting Information Figure S6), which is identical to the SEM observation. Furthermore, based on the TEM images of $\text{Fe}_2\text{O}_3@\text{GS}1$ and $\text{Fe}_2\text{O}_3@\text{GS}2$, it can be found that the graphene sheets were firmly hold the Fe_2O_3 nanoparticles, even after the sonication used to disperse the samples for TEM tests.

To identify the mechanism of the electrochemical reactions, the typical CV profiles of $\text{Fe}_2\text{O}_3@\text{GS}1$ composite and bare Fe_2O_3 for the first, second, and twentieth cycles were measured at a scan rate of 0.5 mV s⁻¹ as shown in Figure 5a and b, respectively. In the cathodic polarization process of the first

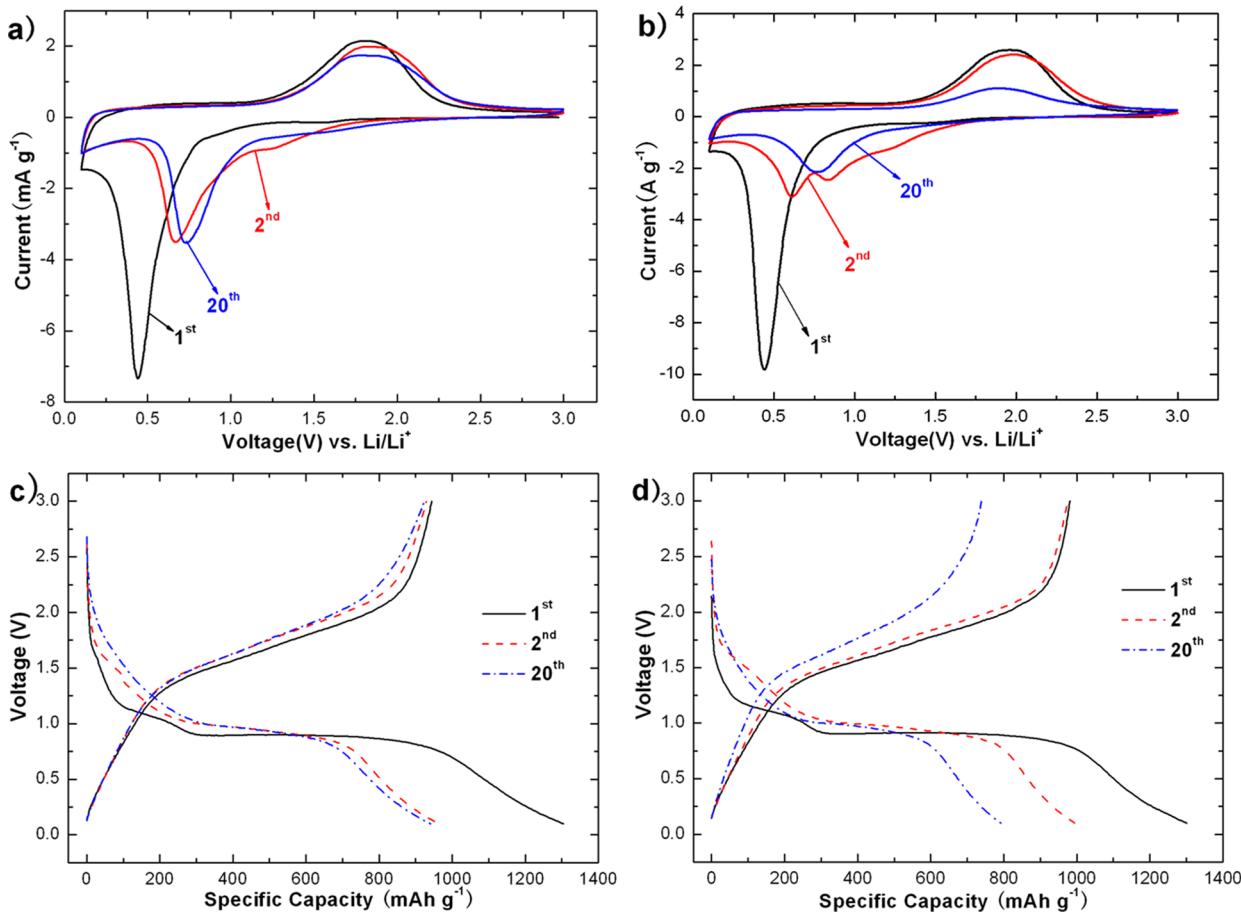


Figure 5. Representative CV curves of (a) Fe_2O_3 @GS1 and (b) bare Fe_2O_3 at a scan rate of 0.5 mV s^{-1} . Charge–discharge curves of (c) Fe_2O_3 @GS1 and (d) bare Fe_2O_3 at a current density of 100 mA g^{-1} between 0.1 and 3.0 V .

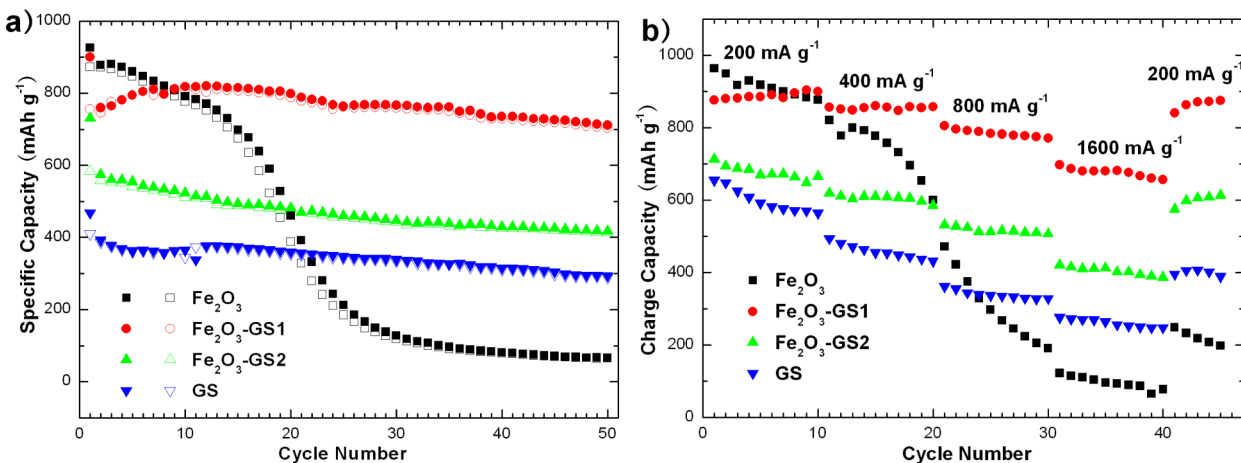


Figure 6. (a) Cycling behavior of pure GS, bare Fe_2O_3 , Fe_2O_3 @GS1, and Fe_2O_3 @GS2 at a current density of 800 mA g^{-1} . Solid and hollow point symbols represent lithium insertion and extraction. (b) Rate performance of pure GS, bare Fe_2O_3 , Fe_2O_3 @GS1, and Fe_2O_3 @GS2 at different current densities.

cycle for Fe_2O_3 @GS1, two peaks, one obvious and one inconspicuous, were observed at about 0.44 and 1.6 V , which were ascribed to the reduction of Fe^{3+} by Li to Fe^0 and the irreversible reaction with the electrolyte, respectively.⁵ Meanwhile, one broadened peak was recorded at about 1.8 V in the anodic process, corresponding to the reversible oxidation of Fe^0 .²⁴ During the subsequent cycles, the cathodic peak potential transfers to about 0.7 V and the CV curves show

good reproducibility except a little decrease in anodic peak intensity, suggesting the good reversible reaction from Fe^0 to Fe^{3+} . For the bare Fe_2O_3 shown in Figure 5b, the current densities and the integrated area of the anodic peaks decrease gradually, indicating the poor reversibility of the reaction from Fe^0 to Fe^{3+} and the capacity loss during the cycling. The electrochemical reversible reaction with Fe_2O_3 anodes could be described as follows:²⁶

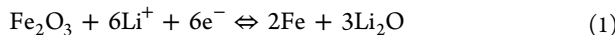


Figure 5c and d show the charge (delithiation) and discharge (lithiation) voltage profiles for the $\text{Fe}_2\text{O}_3@\text{GS1}$ composite and bare Fe_2O_3 at a current density of 100 mA g^{-1} , respectively. Two obvious voltage plateaus located at about 1.6 V (charge) and 0.9 V (discharge) could be observed in the initial charge–discharge curves, which are consistent with the CV results. The first discharge capacities (around 1300 mA h g^{-1}) for both of the two electrodes are much higher than the theoretical capacity of Fe_2O_3 (1007 mA h g^{-1}), which may derive from the decomposition of electrolyte, the formation of the solid electrolyte interface (SEI) layer, and the reduction of oxygenated functional groups on the surface of graphene in the $\text{Fe}_2\text{O}_3@\text{GS1}$ composite.^{8,15} The Coulombic efficiency (CE) of the $\text{Fe}_2\text{O}_3@\text{GS1}$ composite is around 72% at the first cycle, which is close to that of the bare Fe_2O_3 material (75%) and higher than that of individual GS (67%) (Supporting Information Figure S7). After 1 cycle, CE rises to more than 95%. For the $\text{Fe}_2\text{O}_3@\text{GS1}$ electrode, it is notable that no obvious capacity loss was observed after 2 cycles and the electrode could still maintain a reversible capacity of approximately 900 mA h g^{-1} after 20 cycles. In contrast, the reversible capacity of the bare Fe_2O_3 electrode gradually decays to about 800 mA h g^{-1} after 20 cycles.

Figure 6a exhibits the discharge–charge cycling performance of pure GS, bare Fe_2O_3 , $\text{Fe}_2\text{O}_3@\text{GS1}$, and $\text{Fe}_2\text{O}_3@\text{GS2}$ at a current density of 800 mA g^{-1} for 50 cycles. All cells were cycled at a current density of 100 mA g^{-1} for the initial two cycles. The reversible capacity of pure GS gradually decrease from 410 to 289 mA h g^{-1} . The bare Fe_2O_3 shows the high reversible capacity of above 770 mA h g^{-1} for the first 12 cycles, but the capacity starts to decrease dramatically from 13th cycle and only delivers a reversible capacity of 66 mA h g^{-1} after 50 cycles. The reversible capacity for $\text{Fe}_2\text{O}_3@\text{GS2}$ electrode with 30.7% graphene is 417 mA h g^{-1} after 50 cycles and remains 72% of its original value (583 mA h g^{-1}). Nonetheless, the $\text{Fe}_2\text{O}_3@\text{GS1}$ electrode with 12.3% graphene has better cycle performance, showing a high reversible capacity (711 mA h g^{-1}) with the capacity retention of 94% after 50 cycles, which could be attributed to the higher theoretical capacity of $\text{Fe}_2\text{O}_3@\text{GS1}$. Evidently, the $\text{Fe}_2\text{O}_3@\text{GS}$ composites show significantly enhanced cycling performance perhaps benefited from the unique encapsulated structure obtained by the spray drying route.

To further evaluate the electrode kinetics of pure GS, bare Fe_2O_3 , $\text{Fe}_2\text{O}_3@\text{GS1}$ and $\text{Fe}_2\text{O}_3@\text{GS2}$, the rate capacity of the samples is shown in Figure 6b. It is clearly seen that the $\text{Fe}_2\text{O}_3@\text{GS}$ composites, especially the $\text{Fe}_2\text{O}_3@\text{GS1}$ composite with 12.3% graphene, illustrate much better rate performances comparing to the reference GS and Fe_2O_3 . When the current density increases to 1600 mA g^{-1} , the reversible capacity of the $\text{Fe}_2\text{O}_3@\text{GS1}$ composite still keeps a stable value above 660 mA h g^{-1} , which is about 75% of the initial capacity. At this high rate, the GS sample could deliver an average reversible capacity of ca. 260 mA h g^{-1} with 40% of capacity retention. However, the bare Fe_2O_3 electrode displays a noticeably poor rate capability with the increased current densities and the capacity retention is only about 8% after 40 cycles.

In order to clarify the improved electrochemical performance after introducing the graphene into the $\text{Fe}_2\text{O}_3@\text{GS1}$ composite, the Nyquist plots of the AC impedance for the bare Fe_2O_3 and $\text{Fe}_2\text{O}_3@\text{GS1}$ composite were measured after 20 cycles

(Supporting Information Figure S8). The depressed semicircle in the high-medium frequency is related to the charge-transfer resistance on the electrode interface. And the inclined line in the low frequency range represents the Warburg impedance, which corresponds to solid-state diffusion of Li ions within the electrodes. It is evident that the semicircle of the $\text{Fe}_2\text{O}_3@\text{GS1}$ is much smaller than that of the bare Fe_2O_3 electrode, which suggestss that the $\text{Fe}_2\text{O}_3@\text{GS1}$ electrode possesses lower contact and charge-transfer resistance, improved electronic connection of the Fe_2O_3 nanoparticles by effective encapsulation and adherence of highly conductive and flexible GS.

In conclusion, we adopted a simple but effective spray drying method followed by mild heat treatment process to fabricate 3D crumpled GS-wrapped Fe_2O_3 composites as anode materials for LIBs. The as-formed 3D $\text{Fe}_2\text{O}_3@\text{GS}$ composites possesses an open micro/nanostructure, in which nanosized Fe_2O_3 particles are uniformly embedded into the GS matrix and Fe_2O_3 also act as spacers to prevent the closely restacking of GS. The crumpled GS encapsulation not only constitutes 3D continuous and highly conductive network but also provides elastic void spaces to accommodate the strain and stress of the volume change of Fe_2O_3 and avoid the aggregation and pulverization of nano- Fe_2O_3 particles during cycling. And so the synergistic effect between crumpled GS and active nanoparticles is fully utilized. As a result, encapsulation of the 3D crumpled GS significantly enhanced the performance of the Fe_2O_3 in terms of cyclic stability and rate capability. The spray drying technology could be a promising route to massively produce for various high-performance 3D crumpled GS-wrapped composites.

ASSOCIATED CONTENT

Supporting Information

XPS spectra of GO before and after calcination at 220°C for 2 h in air. TGA curves of $\text{Fe}_2\text{O}_3@\text{GS1}$ and $\text{Fe}_2\text{O}_3@\text{GS2}$; EDS mappings and HRTEM images of $\text{Fe}_2\text{O}_3@\text{GS1}$ composite; FESEM and TEM images of $\text{Fe}_2\text{O}_3@\text{GS2}$ composite; Impedance plots for bare Fe_2O_3 and $\text{Fe}_2\text{O}_3@\text{GS1}$ after 20 cycles. This material is available free of charge via the Internet at <http://pubs.acs.org>.

AUTHOR INFORMATION

Corresponding Author

*Tel.: +86-21-54744533. Fax: +86-21-54747717. E-mail: ys-he@sjtu.edu.cn.

Notes

The authors declare no competing financial interest.

ACKNOWLEDGMENTS

We are grateful for the financial support of this work by the National Basic Research Program of China (2007CB209705), the Natural Science Foundation of China (21006063, 21073120, 51272156), the Science and Technology Commission of Shanghai Municipality (10DZ1202702), and the China Scholarship Council Fellowship.

REFERENCES

- Poizot, P.; Laruelle, S.; Gruegeon, S.; Dupont, L.; Tarascon, J. M. Nano-sized transition-metal oxides as negative-electrode materials for lithium-ion batteries. *Nature* **2000**, *407*, 496–499.
- Chen, J.; Xu, L.; Li, W.; Gou, X. α - Fe_2O_3 Nanotubes in Gas Sensor and Lithium-Ion Battery Applications. *Adv. Mater.* **2005**, *17*, 582–586.

- (3) Wu, C.; Yin, P.; Zhu, X.; OuYang, C.; Xie, Y. Synthesis of hematite (α -Fe₂O₃) nanorods: diameter-size and shape effects on their applications in magnetism, lithium ion battery, and gas sensors. *J. Phys. Chem. B* **2006**, *110*, 17806–17812.
- (4) Bruce, P. G.; Scrosati, B.; Tarascon, J. M. Nanomaterials for rechargeable lithium batteries. *Angew. Chem., Int. Ed. Engl.* **2008**, *47*, 2930–2946.
- (5) Chou, S.-L.; Wang, J.-Z.; Wexler, D.; Konstantinov, K.; Zhong, C.; Liu, H.-K.; Dou, S.-X. High-surface-area α -Fe₂O₃/carbon nanocomposite: one-step synthesis and its highly reversible and enhanced high-rate lithium storage properties. *J. Mater. Chem.* **2010**, *20*, 2092–2098.
- (6) Hassan, M. F.; Rahman, M. M.; Guo, Z. P.; Chen, Z. X.; Liu, H. K. Solvent-assisted molten salt process: A new route to synthesise α -Fe₂O₃/C nanocomposite and its electrochemical performance in lithium-ion batteries. *Electrochim. Acta* **2010**, *55*, 5006–5013.
- (7) Yu, W. J.; Hou, P. X.; Zhang, L. L.; Li, F.; Liu, C.; Cheng, H. M. Preparation and electrochemical property of Fe₂O₃ nanoparticles-filled carbon nanotubes. *Chem. Commun. (Camb.)* **2010**, *46*, 8576–8578.
- (8) Chou, S. L.; Wang, J. Z.; Chen, Z. X.; Liu, H. K.; Dou, S. X. Hollow hematite nanosphere/carbon nanotube composite: mass production and its high-rate lithium storage properties. *Nanotechnology* **2011**, *22*, 265401.
- (9) Zhao, Y.; Li, J.; Ding, Y.; Guan, L. Single-walled carbon nanohorns coated with Fe₂O₃ as a superior anode material for lithium ion batteries. *Chem. Commun. (Camb.)* **2011**, *47*, 7416–7418.
- (10) Nagao, M.; Otani, M.; Tomita, H.; Kanzaki, S.; Yamada, A.; Kanno, R. New three-dimensional electrode structure for the lithium battery: Nano-sized γ -Fe₂O₃ in a mesoporous carbon matrix. *J. Power Sources* **2011**, *196*, 4741–4746.
- (11) Zhou, G.; Wang, D.-W.; Li, F.; Zhang, L.; Li, N.; Wu, Z.-S.; Wen, L.; Lu, G. Q.; Cheng, H.-M. Graphene-wrapped Fe₃O₄ anode material with improved reversible capacity and cyclic stability for lithium ion batteries. *Chem. Mater.* **2010**, *22*, 5306–5313.
- (12) Stankovich, S.; Dikin, D. A.; Domke, G. H.; Kohlhaas, K. M.; Zimney, E. J.; Stach, E. A.; Pineri, R. D.; Nguyen, S. T.; Ruoff, R. S. Graphene-based composite materials. *Nature* **2006**, *442*, 282–286.
- (13) Stankovich, S.; Dikin, D. A.; Pineri, R. D.; Kohlhaas, K. A.; Kleinhammes, A.; Jia, Y.; Wu, Y.; Nguyen, S. T.; Ruoff, R. S. Synthesis of graphene-based nanosheets via chemical reduction of exfoliated graphite oxide. *Carbon* **2007**, *45*, 1558–1565.
- (14) Rao, C. N.; Sood, A. K.; Subrahmanyam, K. S.; Govindaraj, A. Graphene: the new two-dimensional nanomaterial. *Angew. Chem., Int. Ed. Engl.* **2009**, *48*, 7752–7777.
- (15) He, Y.-S.; Gao, P.; Chen, J.; Yang, X.; Liao, X.-Z.; Yang, J.; Ma, Z.-F. A novel bath lily-like graphene sheet-wrapped nano-Si composite as a high performance anode material for Li-ion batteries. *RSC Adv.* **2011**, *1*, 958–960.
- (16) He, Y.-S.; Bai, D.-W.; Yang, X.; Chen, J.; Liao, X.-Z.; Ma, Z.-F. A Co(OH)₂-graphene nanosheets composite as a high performance anode material for rechargeable lithium batteries. *Electrochim. Commun.* **2010**, *12*, 570–573.
- (17) Guo, W.; Yin, Y.-X.; Xin, S.; Guo, Y.-G.; Wan, L.-J. Superior radical polymer cathode material with a two-electron process redox reaction promoted by graphene. *Energy Environ. Sci.* **2012**, *5*, 5221–5225.
- (18) Song, Z.; Xu, T.; Gordin, M. L.; Jiang, Y. B.; Bae, I. T.; Xiao, Q.; Zhan, H.; Liu, J.; Wang, D. Polymer-graphene nanocomposites as ultrafast-charge and -discharge cathodes for rechargeable lithium batteries. *Nano Lett.* **2012**, *12*, 2205–2211.
- (19) Zhou, X.; Wang, F.; Zhu, Y.; Liu, Z. Graphene modified LiFePO₄ cathode materials for high power lithium ion batteries. *J. Mater. Chem.* **2011**, *21*, 3353–3358.
- (20) Zhang, M.; Qu, B.; Lei, D.; Chen, Y.; Yu, X.; Chen, L.; Li, Q.; Wang, Y.; Wang, T. A green and fast strategy for the scalable synthesis of Fe₂O₃/graphene with significantly enhanced Li-ion storage properties. *J. Mater. Chem.* **2012**, *22*, 3868–3874.
- (21) Mao, S.; Wen, Z.; Kim, H.; Lu, G.; Hurley, P.; Chen, J. A general approach to one-pot fabrication of crumpled graphene-based nano-hybrids for energy applications. *ACS Nano* **2012**, *6*, 7505–7513.
- (22) Luo, J.; Zhao, X.; Wu, J.; Jang, H. D.; Kung, H. H.; Huang, J. Crumpled graphene-encapsulated Si nanoparticles for lithium ion battery anodes. *J. Phys. Chem. Lett.* **2012**, *3*, 1824–1829.
- (23) Liu, S. Y.; Xie, J.; Pan, Q.; Wu, C. Y.; Cao, G. S.; And, T. J. Z.; Zhao, X. B. Graphene anchored with nanocrystal Fe₂O₃ with improved electrochemical Li-storage properties. *Int. J. Electrochem. Sci.* **2012**, *7*, 354–362.
- (24) Zou, Y.; Kan, J.; Wang, Y. Fe₂O₃-graphene rice-on-sheet nanocomposite for high and fast lithium ion storage. *J. Phys. Chem. C* **2011**, *115*, 20747–20753.
- (25) Zhu, X. J.; Zhu, Y. W.; Murali, S.; Stollers, M. D.; Ruoff, R. S. Nanostructured reduced graphene oxide/Fe₂O₃ composite as a high-performance anode material for lithium ion batteries. *ACS Nano* **2011**, *5*, 3333–3338.
- (26) Zhu, J.; Zhu, T.; Zhou, X.; Zhang, Y.; Lou, X. W.; Chen, X.; Zhang, H.; Hng, H. H.; Yan, Q. Facile synthesis of metal oxide/reduced graphene oxide hybrids with high lithium storage capacity and stable cyclability. *Nanoscale* **2011**, *3*, 1084–1089.
- (27) Zhou, W.; Zhu, J.; Cheng, C.; Liu, J.; Yang, H.; Cong, C.; Guan, C.; Jia, X.; Fan, H. J.; Yan, Q.; Li, C. M.; Yu, T. A general strategy toward graphene@metal oxide core–shell nanostructures for high-performance lithium storage. *Energy Environ. Sci.* **2011**, *4*, 4954–4961.
- (28) Xue, X.-Y.; Ma, C.-H.; Cui, C.-X.; Xing, L.-L. High lithium storage performance of α -Fe₂O₃/graphene nanocomposites as lithium-ion battery anodes. *Solid State Sci.* **2011**, *13*, 1526–1530.
- (29) Zhang, W.; Zeng, Y.; Xiao, N.; Hng, H. H.; Yan, Q. One-step electrochemical preparation of graphene-based heterostructures for Li storage. *J. Mater. Chem.* **2012**, *22*, 8455–8461.
- (30) Bai, S.; Chen, S.; Shen, X.; Zhu, G.; Wang, G. Nanocomposites of hematite (α -Fe₂O₃) nanospindles with crumpled reduced graphene oxide nanosheets as high-performance anode material for lithium-ion batteries. *RSC Advances* **2012**, *2*, 10977–10984.
- (31) Tian, L.; Zhuang, Q.; Li, J.; Wu, C.; Shi, Y.; Sun, S. The production of self-assembled Fe₂O₃–graphene hybrid materials by a hydrothermal process for improved Li-cycling. *Electrochim. Acta* **2012**, *65*, 153–158.
- (32) Chen, D.; Ji, G.; Ma, Y.; Lee, J. Y.; Lu, J. Graphene-encapsulated hollow Fe₃O₄ nanoparticle aggregates as a high-performance anode material for lithium ion batteries. *ACS Appl. Mater. Interfaces* **2011**, *3*, 3078–3083.
- (33) Wang, Y.; Shi, Z.; Huang, Y.; Ma, Y.; Wang, C.; Chen, M.; Chen, Y. Supercapacitor devices based on graphene materials. *J. Phys. Chem. C* **2009**, *113*, 13103–13107.
- (34) Yang, X.; Qiu, L.; Cheng, C.; Wu, Y.; Ma, Z. F.; Li, D. Ordered gelation of chemically converted graphene for next-generation electroconductive hydrogel films. *Angew. Chem., Int. Ed. Engl.* **2011**, *50*, 7325–7328.
- (35) Yang, X.; Zhu, J.; Qiu, L.; Li, D. Bioinspired effective prevention of restacking in multilayered graphene films: towards the next generation of high-performance supercapacitors. *Adv. Mater.* **2011**, *23*, 2833–2838.
- (36) Wang, J. Z.; Zhong, C.; Wexler, D.; Idris, N. H.; Wang, Z. X.; Chen, L. Q.; Liu, H. K. Graphene-encapsulated Fe₃O₄ nanoparticles with 3D laminated structure as superior anode in lithium ion batteries. *Chem.—Eur. J.* **2011**, *17*, 661–667.
- (37) Chen, W.; Li, S.; Chen, C.; Yan, L. Self-assembly and embedding of nanoparticles by *in situ* reduced graphene for preparation of a 3D graphene/nanoparticle aerogel. *Adv. Mater.* **2011**, *23*, 5679–5683.
- (38) Chen, K.; Chen, L.; Chen, Y.; Bai, H.; Li, L. Three-dimensional porous graphene-based composite materials: electrochemical synthesis and application. *J. Mater. Chem.* **2012**, *22*, 20968–20976.
- (39) Wang, G.; Wang, B.; Wang, X.; Park, J.; Dou, S.; Ahn, H.; Kim, K. Sn/graphene nanocomposite with 3D architecture for enhanced reversible lithium storage in lithium ion batteries. *J. Mater. Chem.* **2009**, *19*, 8378–8384.

- (40) Jang, H. D.; Kim, S. K.; Chang, H.; Roh, K. M.; Choi, J. W.; Huang, J. A glucose biosensor based on TiO₂-graphene composite. *Biosens. Bioelectron.* **2012**, *38*, 184–188.
- (41) Chen, D.; Wei, W.; Wang, R.; Zhu, J.; Guo, L. α -Fe₂O₃ nanoparticles anchored on graphene with 3D quasi-laminated architecture: in situ wet chemistry synthesis and enhanced electrochemical performance for lithium ion batteries. *New J. Chem.* **2012**, *36*, 1589–1595.
- (42) Kim, J.-W.; Shin, M.-S.; Kim, J.-K.; Kim, H.-S.; Koo, K.-K. Evaporation crystallization of RDX by ultrasonic spray. *Ind. Eng. Chem. Res.* **2011**, *50*, 12186–12193.
- (43) Kramek-Romanowska, K.; Odziomek, M.; Sosnowski, T. R.; Gradoń, L. Effects of process variables on the properties of spray-dried mannitol and mannitol/disodium cromoglycate powders suitable for drug delivery by inhalation. *Ind. Eng. Chem. Res.* **2011**, *50*, 13922–13931.
- (44) Luo, J.; Jang, H. D.; Sun, T.; Xiao, L.; He, Z.; Katsoulidis, A. P.; Kanatzidis, M. G.; Gibson, J. M.; Huang, J. Compression and aggregation-resistant particles of crumpled soft sheets. *ACS Nano* **2011**, *5*, 8943–8949.
- (45) Ruoff, R. Perspective: A means to an end. *Nature* **2012**, *483*, S42.
- (46) Srivastava, M.; Ojha, A. K.; Chaubey, S.; Singh, J.; Sharma, P. K.; Pandey, A. C. Investigation on magnetic properties of α -Fe₂O₃ nanoparticles synthesized under surfactant-free condition by hydrothermal process. *J. Alloy. Compd.* **2010**, *500*, 206–210.
- (47) Booth, T. J.; Blake, P.; Nair, R. R.; Jiang, D.; Hill, E. W.; Bangert, U.; Bleloch, A.; Gass, M.; Novoselov, K. S.; Katsnelson, M. I.; Geim, A. K. Macroscopic graphene membranes and their extraordinary stiffness. *Nano Lett.* **2008**, *8*, 2442–2446.
- (48) Tang, H.; Ehlert, G. J.; Lin, Y.; Sodano, H. A. Highly efficient synthesis of graphene nanocomposites. *Nano Lett.* **2012**, *12*, 84–90.
- (49) Chen, H.; Müller, M. B.; Gilmore, K. J.; Wallace, G. G.; Li, D. Mechanically strong, electrically conductive, and biocompatible graphene paper. *Adv. Mater.* **2008**, *20*, 3557–3561.
- (50) Huang, Z.-D.; Zhang, B.; Oh, S.-W.; Zheng, Q.-B.; Lin, X.-Y.; Yousefi, N.; Kim, J.-K. Self-assembled reduced graphene oxide/carbon nanotube thin films as electrodes for supercapacitors. *J. Mater. Chem.* **2012**, *22*, 3591.
- (51) Kim, J.; Cote, L. J.; Kim, F.; Huang, J. Visualizing graphene based sheets by fluorescence quenching microscopy. *J. Am. Chem. Soc.* **2010**, *132*, 260–7.
- (52) Jang, H. D.; Kim, S. K.; Chang, H.; Choi, J.-W.; Luo, J.; Huang, J. One-step synthesis of Pt-nanoparticles-laden graphene crumples by aerosol spray pyrolysis and evaluation of their electrocatalytic activity. *Aerosol. Sci. Tech.* **2013**, *47*, 93–98.

■ NOTE ADDED AFTER ASAP PUBLICATION

After this paper was published online December 31, 2012, a correction was made to the text. The corrected version was reposted January 8, 2013.